

AGAINST THE WIND: RADIO LIGHT CURVES OF TYPE IA SUPERNOVAE INTERACTING WITH
LOW-DENSITY CIRCUMSTELLAR SHELLS

CHELSEA E. HARRIS

Astronomy Department, University of California Berkeley, Berkeley, CA

PETER E. NUGENT

Astronomy Department, University of California Berkeley, Berkeley, CA and
Lawrence Berkeley National Laboratory, Berkeley, CA

AND

DANIEL N. KASEN

Astronomy Department, University of California Berkeley, Berkeley, CA and
Lawrence Berkeley National Laboratory, Berkeley, CA*Draft version April 4, 2016*

ABSTRACT

For decades, a wide variety of observations spanning the radio through optical and on to the x-ray have attempted to uncover signs of type Ia supernovae (SNe Ia) interacting with a circumstellar medium (CSM). The goal of these studies is to constrain the nature of the hypothesized SN Ia mass-donor companion. A continuous CSM is typically assumed when interpreting observations of interaction. However, while such models have been successfully applied to core-collapse SNe, the assumption of continuity may not be accurate for SNe Ia, as shells of CSM could be formed by pre-supernova eruptions (novae). In this work, we model the interaction of SNe with a spherical, low density, finite-extent CSM and create a suite of synthetic radio synchrotron light curves. We find that CSM shells produce sharply peaked light curves, and identify a fiducial set of models that all obey a common evolution and can be used to generate radio light curves for interaction with an arbitrary shell. The relations obeyed by the fiducial models can be used to deduce CSM properties from radio observations; we demonstrate this by applying them to the non-detections of SN 2011fe and SN 2014J. Finally, we explore a multiple shell CSM configuration and describe its more complicated dynamics and resultant radio light curves.

Subject headings:

1. INTRODUCTION

A type Ia supernova (SN Ia) is the explosion of a carbon-oxygen white dwarf (Nugent et al. 2011; Bloom et al. 2012). It is hypothesized that in order to explode, these stars need to gain mass from a companion star via some mass transfer mechanism, be it Roche lobe overflow, winds, merger, or something more exotic. The zoo of possible mass transfer mechanisms results in a similar plethora of companion candidates from white dwarfs to red giants. To date, there has never been a direct detection of a normal SN Ia companion (Cao et al. 2015); but there are indirect methods of constraining the companion identity. One method is to search for signs of the ejecta impacting a circumstellar medium (CSM) produced during mass transfer, pre-supernova outbursts, or stellar winds. The ejecta-CSM interaction radiates across a broad range of the spectrum, from x-ray to radio. The CSM composition and structure will reflect the nature of the progenitor system. We refer to any supernova with CSM interaction as an “iSN”. Observations of iSNe are often interpreted through the Chevalier (1982) self-similar model of shock evolution. This model has successfully been used to fit radio light curves of core-collapse radio supernovae (e.g. Chevalier 1996; Marcaide et al. 1997; Soderberg et al. 2008), supporting the hy-

pothesis that the signal is from interaction of the SN ejecta with a wind. The key to the model’s success in that case is that the CSM is extensive and close to the stellar surface, so the shock evolves to the self-similar solution before observations begin.

In the case of iSNe Ia, the density profile of the CSM is unconstrained by both observations and theory. Observations so far have been used to derive upper limits on the density of *continuous* CSM (Panagia et al. 2006; Margutti et al. 2012; Chomiuk et al. 2012; Silverman et al. 2013). However, SN Ia progenitor models come in numerous flavors, many of which do not predict a wind-profile CSM or even a continuous CSM. For instance, a dense CSM shell close to the progenitor white dwarf has been considered to explain high velocity features in SN Ia spectra (Gerardy et al. 2004; Silverman et al. 2015a). Several progenitors models suggest that nova outbursts will sweep CSM into a shell of small radial extent (e.g. Patat et al. 2011; Wood-Vasey & Sokoloski 2006; Moore & Bildsten 2012).

It is the purpose of this work to characterize the radio light curves of supernovae interacting with CSM in a shell. We restrict our studies to the case of low-density CSM such that the interaction is in the adiabatic, optically thin limit. We also assume, unless stated otherwise, that there is negligible CSM interaction prior to interaction with the CSM shell. These assumptions are

consistent with the fact that the majority of SNe Ia show no signs of interaction: if present, CSM must be of low density.

The paper is organized as follows. In the next section we describe our model assumptions and guide the reader through our fiducial model set, which is defined by the ratio of the CSM and ejecta densities at the initial contact point, motivated by Chevalier (1982). In § 3 we present our calculated radio synchrotron light curves for the fiducial set, demonstrate their similarity, and provide a system for parameterizing these light curves such that CSM properties could be easily deduced from a well-observed light curve. Then in § 4 we relax the assumption that the CSM and ejecta densities start in the ratio that defines the fiducial set, and show that the fiducial model relations can still be used to approximate CSM properties even for these models. With that in mind, in § 5 we use our fiducial model light curves to analyze the probability of detecting shells in recent radio observations, given that there are gaps between observations. Finally, in § 6 we illustrate that a system with two shells will, upon collision with the second shell, produce a light curve that is significantly different from the single-shell light curves. The appendices provide the derivations of the radiation equations used in this work.

2. DESCRIPTION OF MODELS AND UNDERLYING ASSUMPTIONS

In this section we briefly describe the hydrodynamic code used for this study and describe the “fiducial model set”.

To model the shell interactions, we used the 1D spherically symmetric Lagrangian hydrodynamics code of Roth & Kasen (2015). The code solves the Euler equations using a standard staggered-grid Von Neumann-Richtmyer technique, and includes an artificial viscosity term to damp out post-shock oscillations (see e.g. Castor 2007). Although this code can treat radiative transport via Monte Carlo methods, we did not exercise the radiation capabilities in this paper. Instead our calculations are purely hydrodynamical with an adiabatic index of an ideal gas, $\gamma = 5/3$, as radiative losses are small for the CSM densities considered here. Figure 1 shows that our models indeed do not trap radiation and do not cool, based on the equations provided in Appendix A.1.

The exact number of resolution elements (“zones”) used in these calculations varied by model but was of order $\sim 10^4$. As described below, the ejecta density profile has an “inner” and “outer” region; the outer ejecta interacts with the CSM and is important for the hydrodynamics. We asserted that the outer ejecta and CSM zones had the same mass resolution. In most models we include a region of “vacuum” outside the CSM shell, and in some models we include zones of inner ejecta. These regions act as buffers to ensure that the shock front does not reach the grid boundary and create numerical artifacts. The vacuum region is constant density at least a factor of 10^3 less dense than the rest of the model, and the inner ejecta is much denser than the rest; therefore resolution matching is infeasible in these regions and they are assigned 3×10^3 zones each when present.

The hydrodynamics code outputs files containing tables of gas properties at user-defined, linearly-spaced time intervals. We call these output files “snapshots”,

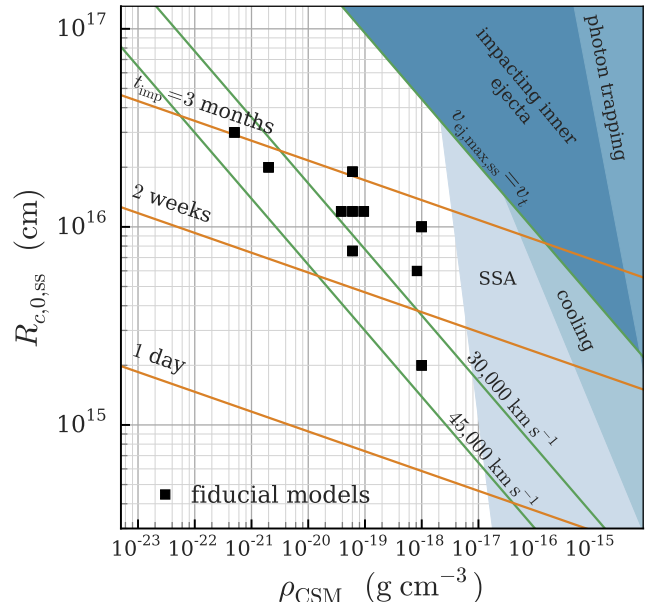


FIG. 1.— A visual representation of the fiducial models presented in this work (black squares) and assumptions (Appendices A.1 and A.2.4), depicted in the $\rho_{\text{CSM}} - R_{c,0,ss}$ plane, where ρ_{CSM} is the CSM density and $R_{c,0,ss}$ is the initial contact discontinuity radius for a fiducial model (Equation 5). Note that models of different shell fractional width (Equation 3) occupy the same position in this space. Lines of constant impact time, t_{imp} (orange), and maximum ejecta velocity, $v_{\text{ej,max,ss}}$ (Equation 16; green), are derived from Equation 5. Shaded regions show where our assumptions would be violated: when the shock region is optically thick to electron scattering and traps photons ($t_{\text{diff}} \geq 0.01 t_{\text{dyn}}$), the shocked gas cools ($t_{\text{cool}} \geq 100 t_{\text{dyn}}$), the CSM impacts dense inner ejecta instead of outer ejecta layers ($v_{\text{ej,max,ss}} > v_t$, Equation 2), or the light curve is altered by synchrotron self-absorption (SSA; $\tau_{\text{SSA}} > 1$ for $T = 10^9$ K and $\nu = 4.9$ GHz, Equation A41).

and they represent only a subset of the numerical time steps taken by the code. Note that, in general, snapshots are taken at different times since explosion for each model. Therefore we linearly interpolate if we wish to know a model property at a specific time, introducing a small interpolation error.

2.1. The Fiducial Model Set

Previous work on CSM interaction has used the self-similar formalism of Chevalier (1982) (hereafter, C82). In that model, freely expanding ejecta described by a power law density profile $\rho_{\text{ej}} = g^n t^{n-3} r^{-n}$ runs into stationary CSM with density $\rho_{\text{CSM}} = q r^{-s}$. The notations of these expressions are as in C82: g and q are scaling parameters, t is the time since explosion, r the distance from the supernova center, and n and s are the power law indices describing the interacting media. The self-similar evolution allows various quantities, including shock position and velocity, to be simply calculated at any time. This formalism has been applied to various core-collapse supernova data with favorable results, and for this reason, as well as its ease of use, the C82 framework is prevalent in studies of iSNe. The well-deserved popularity of this model has motivated its use as a foundation for the “fiducial model set” of this study.

Following C82, we adopt power law density profiles for both the ejecta and the CSM. For the ejecta, we use a

broken power law profile (Chevalier & Fransson 1994), which provides a reasonable approximation to the structure found in hydrodynamical models of SNe. For SN Ia models, Kasen (2010) suggest $\rho \propto r^{-1}$ interior to the transition velocity (v_t) and $\rho \propto r^{-10}$ exterior. We are primarily interested in the outer ejecta ($v > v_t$), which has a density profile

$$\rho_{\text{ej}}(r) = \frac{0.124 M_{\text{ej}}}{(v_t t)^3} \left(\frac{r}{v_t t} \right)^{-10}, \quad (1)$$

$$v_t = (1.014 \times 10^4 \text{ km s}^{-1}) (E_{51}/M_c), \quad (2)$$

where $M_c = M_{\text{ej}}/M_{\text{Ch}}$ is ejecta mass in units of the Chandrasekhar mass and $E_{51} = E/(10^{51} \text{ erg})$ is the explosion energy (in this work, we take $M_{\text{ej}} = 1.38 M_{\odot}$ and $E_{51} = 1$). We assume that the power-law profile of the ejecta extends to a maximum velocity, $v_{\text{ej,max}}$, above which the density drops off precipitously. The ejecta is initially freely expanding with uniform temperature $T_{\text{ej}} = 10^4 \text{ K}$; the value of the preshock ejecta temperature does not play a significant role in the evolution of the shocked gas.

The CSM is taken to be confined to a shell with an inner radius, $R_{c,0}$, and width ΔR_{CSM} . We define the *fractional width*, f_R , as

$$\Delta R_{\text{CSM}} \equiv f_R R_{c,0}. \quad (3)$$

In this work a “thin” shell is a shell with $f_R = 0.1$ and a “thick” shell has $f_R = 1$. For example, Moore & Bildsten (2012) predict $f_R \approx 0.1$ for the shells swept up by nova outbursts. In our calculations, we assume that there is no CSM interior to $R_{c,0}$.

The CSM at the start of our simulation (the time of impact) is constant density ($s = 0$), constant velocity ($v_{\text{CSM}} = 1 \text{ km s}^{-1}$), and isothermal ($T_{\text{CSM}} = 10^3 \text{ K}$). The chosen value of v_{CSM} is arbitrary and unimportant as long as it is much less than the ejecta velocities. Observations of variable narrow absorption features in SN Ia spectra demonstrate the possibility of moderate velocities, such as $v_{\text{CSM}} \sim 65 \text{ km s}^{-1}$ in PTF 11kx (Dilday et al. 2012).

The ejecta impacts the shell at time t_{imp} after explosion. In our set of fiducial models, we set initial conditions such that the ratio of ρ_{CSM} to ρ_{ej} at the contact discontinuity is a fixed value. Physically, our motivation is that the interaction typically becomes most prominent once $\rho_{\text{ej}} \sim \rho_{\text{CSM}}$. The value we use is $\rho_{\text{CSM}}/\rho_{\text{ej}} = 0.33$ so that the initial contact discontinuity radius $R_{c,0}$ corresponds to the C82 contact discontinuity radius at the time of impact (Equation 3 of C82)

$$R_{c,0,\text{ss}} = \left[A_R \left(\frac{g^n t^{n-3}}{q} \right) \right]^{1/(n-s)} \quad (4)$$

$$= (0.041 M_{\text{ej}} v_t^7)^{0.1} t_{\text{imp}}^{0.7} \rho_{\text{CSM}}^{-0.1} \quad (5)$$

$$= (5.850 \times 10^{14} \text{ cm}) \left(\frac{t_{\text{imp}}}{\text{day}} \right)^{0.7} \rho_{\text{CSM},-18}^{-0.1}, \quad (6)$$

where $A_R = 0.33 = \rho_{\text{CSM}}/\rho_{\text{ej}}$ (for $n = 10, s = 0$) and $\rho_{\text{CSM},-18} = \rho_{\text{CSM}}/(10^{-18} \text{ g cm}^{-3})$; because of this connection to the C82 self-similar solution, we use the subscript “ss” in this work to note when this constraint on

the initial conditions is in place. Although our calculations do not assume a self-similar structure, restricting our initial setup in this way turns out to produce a family of light curve models that are amenable to simple parameterization. We explore calculations with different initial conditions in § 4.

Equation 5 shows that, within the fiducial model set, choosing $R_{c,0}$ and ρ_{CSM} fixes the impact time t_{imp} , and hence the maximum ejecta velocity $v_{\text{ej,max}} = R_{c,0}/t_{\text{imp}}$. Figure 1 illustrates the values of $R_{c,0,\text{ss}}$ and ρ_{CSM} shown in this work, and shows that the fiducial model set obeys the assumptions of transparency and lack of radiative cooling (quantified in A.1).

Figure 2 shows the evolution of the energy and mass density profiles for a supernova impacting a typical $f_R = 0.1$ shell model. Immediately before impact (panel A), the CSM has low energy density, a flat density profile, and is moving slowly. The interaction creates a forward shock moving into the CSM, and a reverse shock propagating backwards into the ejecta. The forward shock eventually reaches the outer edge of the shell at a time we call “shock breakout”. At this time (panel B), the dynamics have not yet reached a self-similar state; the internal energy density of the gas, u_{gas} , is high and the CSM has been accelerated to nearly the ejecta speed. Shock breakout accelerates the CSM such that shortly afterward (panel C), the mass and energy densities have dropped drastically and the outermost CSM has reached speeds over $30,000 \text{ km s}^{-1}$. At a time 1.41 times the impact time (panel D), the velocity profile has approximately returned to the $v \propto r$ of free expansion. The mass and energy density profiles will thereafter decrease according to adiabatic free expansion.

The impact radius constraint $R_{c,0} = R_{c,0,\text{ss}}$ (Equation 5) defines a fiducial set of single-shell interaction models. As we will see in the next section, these models generate a family of light curves from which it is possible to deduce CSM properties.

3. RADIO SYNCHROTRON LIGHT CURVES FOR FIDUCIAL MODEL SET

Radio emission is a tell-tale sign of interaction and commonly used to study astronomical shocks. Here we present radio synchrotron light curves of the models described in the previous section, using the equations given in Appendix A.2.1. These models are restricted to low densities where synchrotron self-absorption is not important (Figure 1). Calculating light curves requires that we parameterize the fraction of postshock energy in magnetic fields, ϵ_B , and in non-thermal relativistic electrons, ϵ_e . We assume constant values typically used in the literature, $\epsilon_B = 0.1, \epsilon_e = 0.1$, but note that these quantities are a main source of uncertainty in predicting the radio emission. Calculating x-ray and optical line signatures of our models is an exciting possibility for future work, but here we wish to focus on illustrating the radio emission produced by shell interaction and how it differs from the commonly applied self-similar model.

We assume that the CSM is of solar composition and that the conditions in the shocked ejecta are such that only the fully-ionized shocked CSM (temperature exceeding 10^4 K) contributes to the synchrotron emission (Chevalier & Fransson 2006; Warren et al. 2005). Representative light curves are shown in Figure 3 for in-

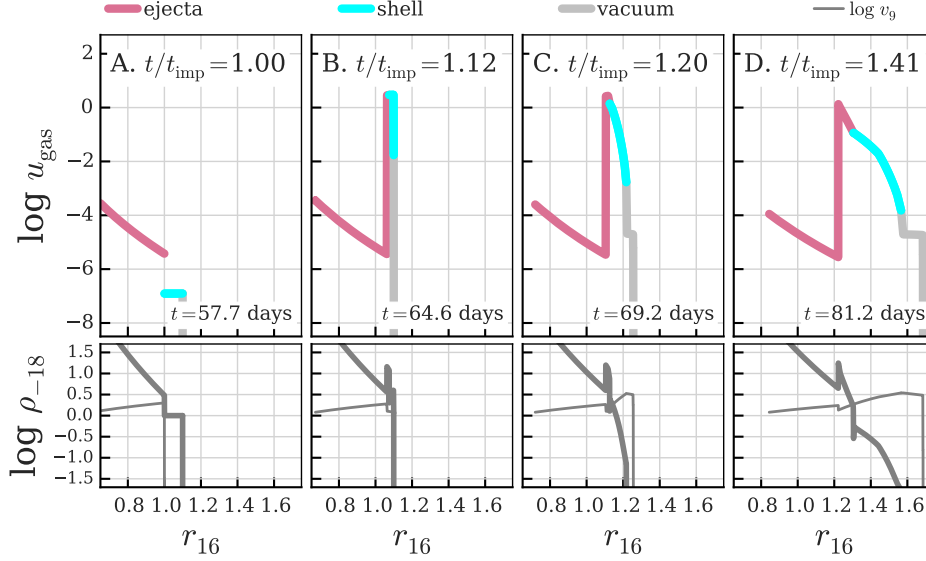


FIG. 2.— The evolution of internal energy density in erg cm^{-3} (log scale, $\log u_{\text{gas}}$; top), mass density per $10^{-18} \text{ g cm}^{-3}$ (log scale, $\log \rho_{-18}$; bottom; thick), and velocity per 10^9 cm s^{-1} (log scale, $\log v_9$; bottom; thin) as a function of radius per 10^{16} cm (linear scale, r_{16}) in a fiducial thin shell impact model ($f_R = 0.1$, $v_{\text{ej,max}} = 20,047 \text{ km s}^{-1}$, $\rho_{\text{CSM}} = 10^{-18} \text{ g cm}^{-3}$, $R_{c,0} = 10^{16} \text{ cm}$). In the top panels, different regions of the model are color-coded: ejecta (pink), CSM (cyan; radiating region), and vacuum (grey). These regions do not mix in our simulations. The times shown are the initial state (A); the moment of shock breakout (B); after shock breakout, before all of the CSM has been accelerated (C); and after significant expansion (D). Labels refer to both the time relative to impact (t_{imp}) and time since explosion (t). We see that energy density, which dominates the shell emissivity (Equation A22), is high while the shock front is in the shell and drops dramatically after shock breakout.

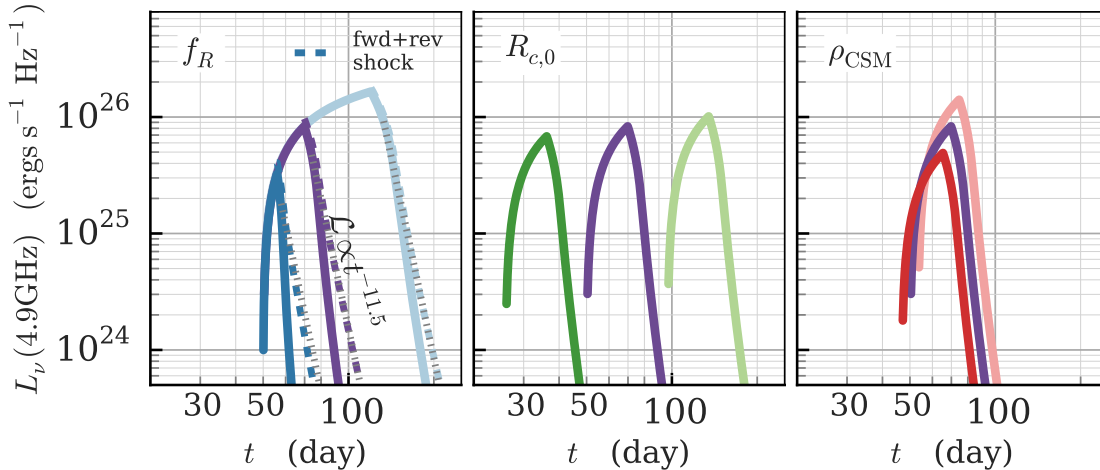


FIG. 3.— Dependence of the fiducial model radio light curves (at 4.9 GHz) on physical parameters. *Left panel:* Effect of varying the shell fractional widths from $f_R = \Delta R_{\text{CSM}}/R_{c,0} = 0.1, 0.316, 1.0$. The light curve peak occurs at shock breakout, so wider shells reach higher luminosities and have broader light curves. The dashed lines show light curve calculations that include emission from the reverse shock region after peak. The dotted grey lines show the empirical fit described in § 3.2. *Center panel:* Effect of varying the initial impact radius from $R_{c,0} = 7.6 \times 10^{15}, 1.2 \times 10^{16}, 1.9 \times 10^{16} \text{ cm}$. Increasing $R_{c,0}$ increases the time of impact, but causes only a small increase in the peak luminosity. *Right panel:* Effect of varying CSM density from $\rho_{\text{CSM}} = 3.8 \times 10^{-20}, 6 \times 10^{-20}, 9.6 \times 10^{-20} \text{ g cm}^{-3}$. Higher densities result in a higher peak luminosity, with a small effect on impact time (as expected from Equation 5).

interactions with shells of various widths, impact radii, and CSM densities. The light curves initially rise as the shock moves through the shell and increases the volume of shocked material (the emission region). The light curves reach a sharp peak, then rapidly decline. The peak occurs at shock breakout, which we define as the moment the radius of the forward shock front reaches the outer radius of the CSM. The rapid decline can be attributed to the plummeting internal energy of the gas as

the shell suddenly accelerates (Figure 2, Equation A21). Changing only the shell width changes the time of shock breakout and therefore wider shells – in which breakout necessarily occurs later – produce broader, brighter light curves. Thinner shells follow the rise of the thicker shells until the time of shock breakout, as expected since the shock evolution should be the same while inside the shell.

In the left panel of Figure 3 we show how including the contribution of the reverse shocked ejecta affects the

radio light curves. We use the same radiation parameters for the ejecta as for the CSM (except we assume metal-rich gas so $Z/A \approx 0.5$ in the calculation of electron density; see Appendix A.2.1). We find that under these assumptions the reverse shock contributes negligibly (about 10%) to the light curve before shock breakout but becomes dominant at later times, when it has a much higher energy density than the CSM (see panel D of Figure 2). However, we stress that it is unclear whether the conditions in the postshock ejecta are the same as in the postshock CSM; emission from the postshock ejecta could be dimmer than we have calculated here if, for instance, this region has a lower value of ϵ_B . Because of the uncertainty in how to treat the ejecta relative to the CSM, in this work we do not include the ejecta when calculating the radio emission unless we explicitly state otherwise.

The distance of the shell from the supernova primarily affects the impact time, as one may expect, and has a small effect on the peak luminosity reached; the density of the shell primarily affects the luminosity and has a small effect on the impact time. When fractional width is held constant as is done when we vary impact radius and shell density, we see that the light curves have the same shape and are simply shifted around in $\log t - \log \mathcal{L}$ space, as can be seen in the middle and right panels of Figure 3.

In Figure 4 we show the light curves of our fiducial suite of numerical models (having different fractional widths, CSM densities, and impact times) normalized by their impact time and early-time luminosity. This view confirms that changing the impact radius and CSM density really does just shift the light curves in log-space and details of the light curve shape are governed by f_R alone.

For reference, we show in Figure 4 the slope of the radio light curve predicted by the self-similar model (Equation A30). While at later times the shell light curves approach the shallow slope of the self-similar model, at most times this slope does not describe the light curve. We also show the decay expected after peak from a simple analytic model that accounts for adiabatic losses in freely expansion gas (Equation A34). The analytic curve is shallower than the decline from our models, as the models accelerate and expand faster than free expansion immediately after shock breakout.

The similarity of the fiducial model set light curves is rooted in fact that the models all have the same value of A_R , the initial ratio between the pre-shock CSM and ejecta density at the contact discontinuity (Equation 5). Our next step is to quantitatively define the family of light curves so that any light curve can be cheaply reconstructed for a given f_R and peak luminosity \mathcal{L}_p .

3.1. Parameterization of Light Curve Peak Time

First, we quantify how the fractional width of the shell, f_R , affects the timescale for the light curve to reach peak, t_p . The peak occurs when the forward shock radius (R_1) is equal to the outer shell radius, $[1 + f_R]R_{c,0}$ (see Equation 3). In the C82 self-similar solution, $R_1 = 1.131R_c$ and $R_c/R_{c,0} = (t/t_{\text{imp}})^{0.7}$ for our choices of $n = 10$ and $s = 0$. This predicts that the time of peak is related to

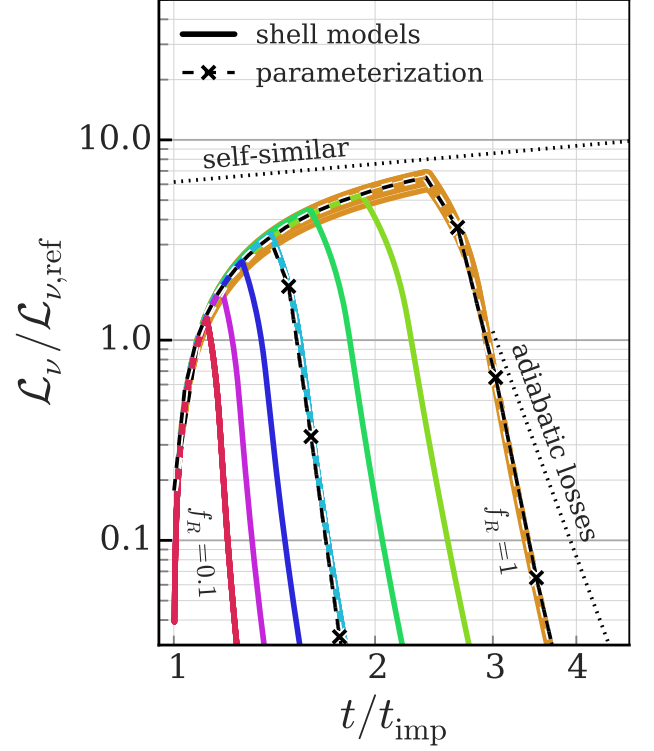


FIG. 4.— Light curves at 4.9 GHz with time normalized to the time of impact, t_{imp} , and luminosity normalized to the luminosity at $1.09t_{\text{imp}}$ ($\mathcal{L}_{\nu,\text{ref}}$), when all light curves are rising. Curves are color coded by shell fractional width, $f_R = \Delta R_{\text{CSM}}/R_{c,0}$, with logarithmic spacing between $f_R = 0.1$ and $f_R = 1$. Multiple models of varying ρ_{CSM} and t_{imp} are shown for $f_R = 0.1, 0.316, 1.0$ (red, cyan, and orange, respectively) to demonstrate that the normalized light curves are nearly identical. Reconstructed light curves based on the empirical parameterization described in §3 are shown for $f_R = 0.316, .01$ (black dashed lines), and provide an excellent approximation to the hydrodynamical model light curves. The slopes predicted for self-similar evolution ($\mathcal{L} \propto t^{0.3}$, Appendix A.2.2) and for free expansion with adiabatic energy loss ($\mathcal{L} \propto t^{-9}$, Appendix A.2.3) are shown as dotted lines with arbitrary normalization; they do not capture the shape of these light curves.

f_R through

$$f_R + 1 = 1.131 \left(\frac{t_p}{t_{\text{imp}}} \right)^{0.7} \Leftrightarrow \frac{t_p}{t_{\text{imp}}} = 0.839(f_R + 1)^{1.43}. \quad (7)$$

If instead the shock is assumed to move at constant velocity (as is true in the early evolution before self-similarity is reached) $R_1/R_{c,0} = t/t_{\text{imp}}$ so $t_p/t_{\text{imp}} = 1 + f_R$.

Figure 5 shows t_p/t_{imp} versus $(f_R + 1)$ for our suite of numerical calculations, which we find are well fit with the power law

$$\frac{t_p}{t_{\text{imp}}} = 1.11 \left(\frac{(f_R + 1)}{1.1} \right)^{1.28}. \quad (8)$$

Unsurprisingly, the exponent $\alpha = 1.28$ lies between the self-similar ($\alpha = 1.43$) and free-expansion ($\alpha = 1$) predictions.

We find empirically that the peak luminosity depends on $R_{c,0}$ and ρ_{CSM} in the way predicted by self-similar evolution (Equation A29) but with a different normal-

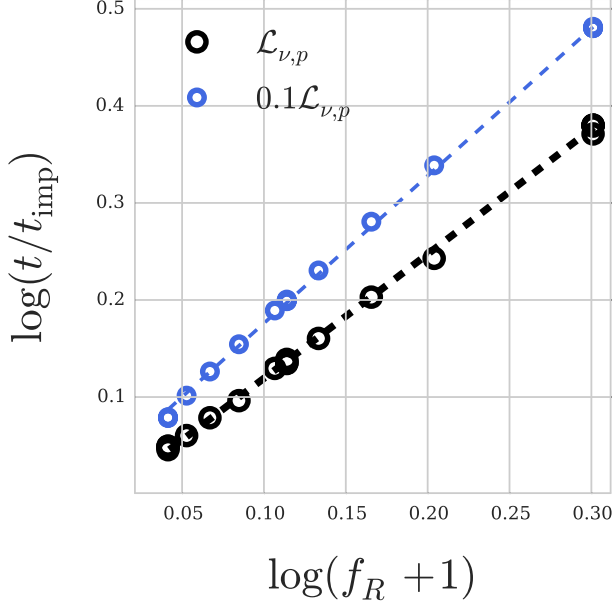


FIG. 5.— Time of peak (black) and time to fall to 10% $\mathcal{L}_{\nu,p}$ (blue) normalized to impact time versus the fractional width of the shell, f_R (Equation 3) for our fiducial model suite (open circles). Broader shells (i.e., higher f_R) have broader light curves (as illustrated in Figure 4). This trend is well fit by a power law (dashed lines), which forms the basis for the parameterization of a fiducial model light curve. Fit parameters for the power law of Equation 13 are given in Table 1.

ization than predicted by that relation. For the $f_R = 1$ light curves the best fit peak luminosity is

$$\mathcal{L}_{\nu,p}|_{f_R=1} \approx (1.9 \times 10^{30} \text{ erg s}^{-1} \text{ Hz}^{-1}) \left(\frac{\nu}{\text{GHz}} \right)^{-1} \times \rho_{\text{CSM},-18}^{8/7} R_{c,0,16}^{3/7} \quad (9)$$

where $R_{c,0,16} = R_{c,0}/(10^{16} \text{ cm})$ is the scaled initial contact discontinuity radius. The peak luminosity of thinner shells – which as we see in Figure 3 peak at a lower luminosity because shock breakout occurs sooner – can be found with a parameterization of the light curve rise, given below.

3.2. Parameterization of Light Curve Rise and Fall Times

To fit the light curve rise, we note that all light curves follow the same rise shape up until the time of peak. A function of the form $\mathcal{L} = a - b/t$ fits the rise of $f_R = 1$ light curves well, with

$$\mathcal{L}_{\nu}(t) = 1.705 \mathcal{L}_{\nu,p}|_{f_R=1} \left[1 - 0.985 \left(\frac{t}{t_{\text{imp}}} \right)^{-1} \right] \quad (10)$$

so using Equation 9 the rise of fiducial model light curves is

$$\mathcal{L}_{\nu}(t) = (3.2 \times 10^{28} \text{ erg s}^{-1} \text{ Hz}^{-1}) \left(\frac{\nu}{\text{GHz}} \right)^{-1} \times \rho_{\text{CSM},-18}^{8/7} R_{c,0,16}^{3/7} \left[1 - 0.985 \left(\frac{t}{t_{\text{imp}}} \right)^{-1} \right] \quad (11)$$

If desired, the peak luminosity of *any* fiducial model

TABLE 1
PARAMETERS FOR EQUATION 13

Luminosity	Q	α
peak		
$\log \mathcal{L}_{\nu,p}$	1.11	1.28
waning		
$\log \mathcal{L}_{\nu,p} - 0.25$	1.16	1.39
$\log \mathcal{L}_{\nu,p} - 1$	1.22	1.52
$\log \mathcal{L}_{\nu,p} - 2$	1.32	1.62
$\log \mathcal{L}_{\nu,p} - 3$	1.48	1.70

NOTE. — Using Q and α in Equation 13 will return the t/t_{imp} , as a function of f_R , at which a given luminosity (first column) is reached.

can be found by substituting Equation 8 in to Equation 11

$$\mathcal{L}_{\nu,p,ss} \approx (3.2 \times 10^{28} \text{ erg s}^{-1} \text{ Hz}^{-1}) \left(\frac{\nu}{\text{GHz}} \right)^{-1} \times \rho_{\text{CSM},-18}^{8/7} R_{c,0,16}^{3/7} [1 - (1 + f_R)^{-1.28}] \quad (12)$$

To describe the light curve decline, we choose four characteristic times along the fall: the time to fall a factor of $10^{-1/4}$ ($\sim 50\%$), 10^{-1} , 10^{-2} , and 10^{-3} of $\mathcal{L}_{\nu,p}$. As demonstrated in Figure 5 for the $\mathcal{L} = 10^{-1} \mathcal{L}_{\nu,p}$ case, these characteristic times follow a power law in $(f_R + 1)$,

$$\frac{t}{t_{\text{imp}}} = Q \left(\frac{f_R + 1}{1.1} \right)^{\alpha} \quad (13)$$

with fit parameters Q and α given in Table 1. Between characteristic points, we interpolate light curves linearly in $\log(\mathcal{L}) - \log(t)$ space (Figure 4).

Putting the parameterized rise and fall expressions together, one can create an approximate light curve for any peak luminosity and shell width; the reconstruction will be a good approximation to the full numerical calculation, as shown in Figure 4. Finally, as mentioned previously, the decline of the light curve is modified when one includes a contribution from the reverse shock (Figure 3). Empirically, we find that the light curve at times later than the characteristic point $10^{-1/4} \mathcal{L}_{\nu,p}$ declines like $\mathcal{L}_{\nu} \propto t^{-11.5}$, which when combined with the equation for time to decline to $10^{-1/4} \mathcal{L}_{\nu,p}$ (Table 1) yields

$$\mathcal{L}_{\nu,(f+r)} = 0.67 \mathcal{L}_{\nu,p} (f_R + 1)^{16} (t/t_{\text{imp}})^{-11.5} \quad (14)$$

where the subscript “f+r” indicates the luminosity of the light curve including both the forward and reverse shock components while $\mathcal{L}_{\nu,p}$ is as given in Equation 12. We illustrate this fit in the left panel of Figure 3.

4. EFFECT OF MAXIMUM EJECTA VELOCITY

In our simulations we must choose an initial radius (equivalently, velocity) at which to truncate the ejecta, $R_{c,0} = v_{\text{ej,max}} t_{\text{imp}}$. The fiducial model set is defined by $R_{c,0} = R_{c,0,ss}$ (Equation 5), so the maximum velocity is

$$v_{\text{ej,max,ss}} = R_{c,0,ss} t_{\text{imp}}^{-1} \quad (15)$$

$$= (2 \times 10^9 \text{ cm s}^{-1}) R_{c,0,16}^{-3/7} \rho_{\text{CSM},-18}^{-1/7} \quad (16)$$

with $R_{c,0,16} = R_{c,0,ss}/(10^{16} \text{ cm})$. Early time spectra of normal SNe Ia show ejecta with maximum velocities

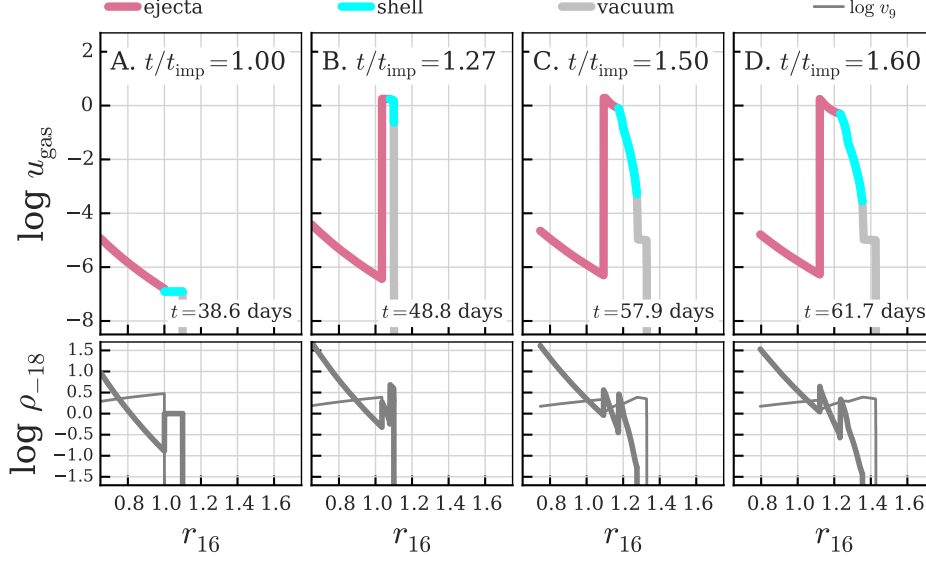


FIG. 6.— Same as Figure 2 but for a “high-velocity” initial conditions model with $v_{\text{ej,max}} = 30,000 \text{ km s}^{-1}$ ($t_{\text{imp}} = 38.6$ days) and the same CSM as in Figure 2. Compared to a fiducial model, the ejecta is less dense at the initial point of contact; so the shock is slower, shock breakout happens later, and the CSM does not gain as much energy.

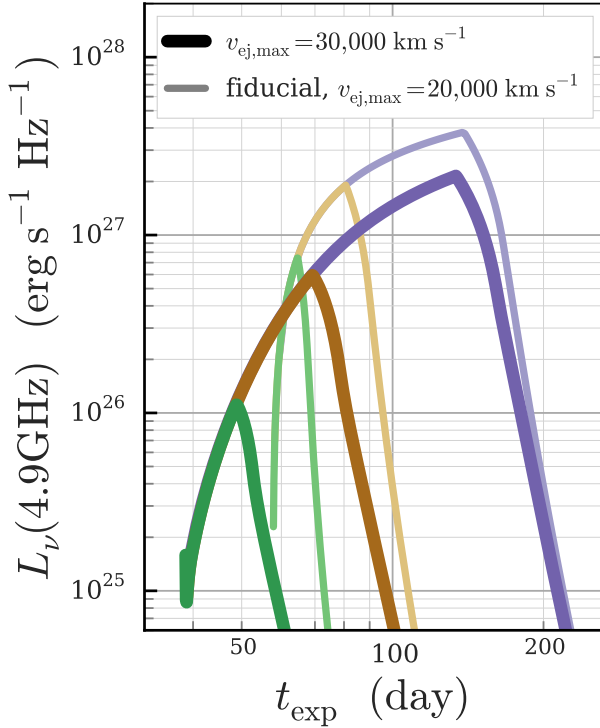


FIG. 7.— Light curves at 4.9 GHz, comparing fiducial models (§2; $t_{\text{imp}} = 57.7$ days, $v_{\text{ej,max}} = 20,000 \text{ km s}^{-1}$, light thin) to “high velocity ejecta” models (§4; $v_{\text{ej,max}} = 30,000 \text{ km s}^{-1}$, $t_{\text{imp}} = 38.6$ days, dark thick). The CSM shell widths shown are: $f_R = 0.1$ (green, narrowest light curves), $f_R = 0.316$ (brown), and $f_R = 1$ (purple, broadest light curves). All models have $\rho_{\text{CSM}} = 10^{-18} \text{ g cm}^{-3}$. Decreasing the ejecta density relative to CSM (i.e. increasing maximum velocity) lowers the peak luminosity and causes the light curve to peak at an earlier time since explosion. However, the effect is negligible for thick shells, and even for thinner shells the fiducial relations can estimate shell properties.

$v_{\text{ej,max}} \approx 30,000 \text{ km s}^{-1}$ (Parrent et al. 2012; Silverman et al. 2015b), and we take $v_{\text{ej,max}} = 45,000 \text{ km s}^{-1}$ as an upper limit. One could constrain oneself to fiducial models in this velocity range, but as illustrated in Figure 1 that is a narrow band of models. Considering that the ejecta velocity is one of the most important constraints on SN Ia explosion models, we wanted to explore the effect of ejecta with $v > v_{\text{ej,max,ss}}$ on our light curves. We call these “high-velocity models”, although they could also be thought of as “super- A_R ” models, as they have a higher initial CSM to ejecta density than the fiducial model value $A_R = 0.33$. Note that these models are not plotted on Figure 1, to avoid confusion regarding the reference lines that apply only to fiducial models.

Figure 6 shows the hydrodynamic evolution for a high-velocity model analogue of the model shown in Figure 2. The fiducial model of Figure 2 was initialized with $\rho_{\text{CSM}} = 10^{-18} \text{ g cm}^{-3}$ and $R_{c,0} = 10^{16} \text{ cm}$, which implies $v_{\text{ej,max}} \approx 20,000 \text{ km s}^{-1}$ and $t_{\text{imp}} = 57.7$ days. The high-velocity model Figure of 6 has the same CSM properties but $v_{\text{ej,max}} = 30,000 \text{ km s}^{-1}$, thus it has $t_{\text{imp}} \approx 38.6$ days ($A_R = 1.00$). The high-velocity model has a lower initial ram pressure, since at a fixed radius $\rho_{\text{ej}} \propto t^7 \propto v^{-7}$ (Equation 1) and $p_{\text{ram}} \propto \rho_{\text{ej}} v^2 \propto v^{-5}$; therefore the forward shock is slower and the light curve takes a few hours longer to reach peak (time of shock breakout; Figure 6, panel B).

Example light curves of high-velocity models with varying f_R are presented in Figure 7, along with their fiducial model counterparts. Including the higher velocity ejecta leads to light curves that are broader, dimmer, and peak earlier. As discussed, the effect on breadth is because the shock is slower so it takes longer to cross the shell. The dimming is also due to the lower shock speed (Equations A9 and A21). That the light curves peak earlier relative to explosion time is simply due to the earlier impact time.

The offsets in peak luminosity and time of peak are

more pronounced in thinner shell models, both in absolute and relative terms. Therefore we decided to apply the fiducial model relations of § 3 to see how well they recover shell properties from the $f_R = 0.1$ high-velocity model. If the $v_{\text{ej,max}} = 30,000 \text{ km s}^{-1}$ light curve had been observed, one would calculate that $f_R = 0.2$ (Equation 8), $\rho_{\text{CSM}} = 1.2 \times 10^{-18} \text{ g cm}^{-3}$, and $R_{c,0} = 7.5 \times 10^{15} \text{ cm}$ (Equations 5 and 12) – all correct to within a factor of a few.

Overall, we conclude that one can still apply the fiducial model relations to an observed light curve to reasonably estimate CSM properties even if the derived parameters yield a $v_{\text{ej,max,ss}}$ that is below the observed ejecta velocity, $v_{\text{ej,o}}$. Therefore, in the next section, we will take the liberty of applying the fiducial relations to the analysis of iSNe Ia radio non-detections.

5. OBSERVATIONAL CONSTRAINTS

In this section we use the radio observations of SN 2011fe from Chomiuk et al. (2012, hereafter CSM12) and of SN 2014J from Pérez-Torres et al. (2014, hereafter PT14) to illustrate how our models can be used to interpret radio nondetections in SNe Ia. As detailed below, we do this by calculating a suite of parameterized light curves relevant to the observations, determining if each would be observed, then converting these observation counts into observation likelihoods.

The analysis begins by defining the set of observations. CSM12 observed SN 2011fe in two bands with effective frequency $\nu = 5.9 \text{ GHz}$ at times after explosion $t_{\text{exp}} = 2.1 - 19.2$ days, with luminosity limits $\sim 10^{24} \text{ erg s}^{-1} \text{ Hz}^{-1}$ for each observation. To interpret these observational constraints, we generate 10^6 light curves corresponding to different interaction models by log-uniform randomly distributed sampling of peak luminosity, shell width, and impact time with values in the range $\mathcal{L}_p(5.9 \text{ GHz}) \in [10^{24}, 10^{27}) \text{ erg s}^{-1} \text{ Hz}^{-1}$, $f_R \in [0.1, 1)$, and $t_{\text{imp}} \in [2, 19)$ days. For each light curve, we then determine if it was observed, i.e. if it was above the CSM12 luminosity limit for any single observation. We restrict ourselves this way since if the shell had been observed it would have affected the observation schedule; but using our models one could interpret stacked data sets as well. Finally, we bin the light curves in f_R and \mathcal{L}_p and in each bin calculate the probability that it would have been observed (the ratio of the number of light curves observed to the number sampled). The probability of the light curve appearing in any single observation is shown in Figure 8.

CSM12 attempted to estimate, without using explicit shell light curve models, the probability of detecting a specific CSM shell. The shell they considered had fractional width $f_R \sim 0.1$, mass $6 \times 10^{-8} M_\odot$ (from a wind of $\dot{M} = 2 \times 10^{-7} M_\odot \text{ yr}^{-1}$), and sat at $R \approx 5 \times 10^{15} \text{ cm}$; the authors estimated a 30% chance of detecting the shell. The preshocked CSM density is

$$\rho_{\text{CSM}} = (4.7 \times 10^{-24} \text{ g cm}^{-3}) M_{-8} R_{16}^{-3} [(1 + f_R)^3 - 1]^{-1} \quad (17)$$

where $M_{-8} = M_{\text{CSM}}/(10^{-8} M_\odot)$ and $R_{16} = R/(10^{16} \text{ cm})$. We estimate that the shell described by CSM12, which has $M_{-8} = 6$, $R_{16} = 0.5$, and $\rho_{\text{CSM}} \approx 7 \times 10^{-22} \text{ g cm}^{-3}$ would have a peak luminosity (Equa-

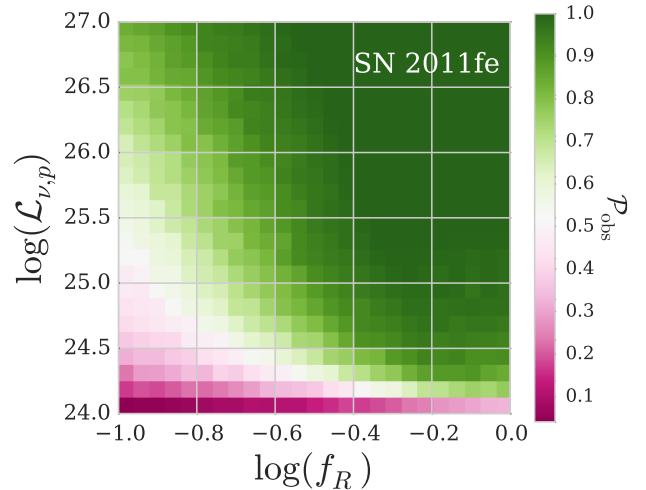


FIG. 8.— Probability that the CSM12 cadence would observe a light curve (\mathcal{P}_{obs}) with peak luminosity $\mathcal{L}_{\nu,p}(5.9 \text{ GHz})$ from a shell of fractional width f_R (Equation 3) for a set of light curves that have log-uniform randomly assigned values of $\mathcal{L}_{\nu,p} \in [10^{24}, 10^{27}) \text{ erg s}^{-1} \text{ Hz}^{-1}$, $f_R \in [0.1, 1)$, and $t_{\text{imp}} \in [2, 19)$ days. For a given f_R and initial shell radius, peak luminosity can be converted into CSM density using Equation 12 as is done in Figure 9 for SN 2014J.

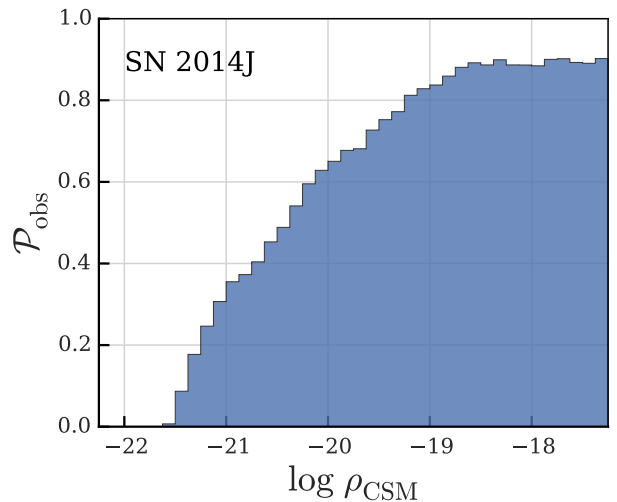


FIG. 9.— Probability (\mathcal{P}_{obs}) that any single radio observation of Pérez-Torres et al. (2014) would detect a thin CSM shell ($f_R = 0.1$) of a given mass density (ρ_{CSM}) around SN 2014J if impact occurred during their observation window, 8.2-35.0 days.

tion 12) $\mathcal{L}_{\nu,p}(5.9 \text{ GHz}) \approx 6 \times 10^{22} \text{ erg s}^{-1} \text{ Hz}^{-1}$, and would be undetected in their observations. For reference we note that at our assumed distance and width, a shell would need to have $M_{-8} \approx 600$ to have $\sim 50\%$ chance of detection.

For SN 2014J, we will demonstrate how one can instead analyze the probability of observing a shell of a given density, rather than peak luminosity. The observations of SN 2014J by Pérez-Torres et al. (2014) span the range 8.2-35.0 days. Using the observation times, frequencies, and limits from PT14 Table 1, we perform the same random sampling test as for SN 2011fe described above, but with a peak luminosity range $10^{23-28} \text{ erg s}^{-1} \text{ Hz}^{-1}$ at

1.55 GHz (their lowest frequency band) and impact times between 2 and 35 days. Isolating the $f_R = 0.1$ bin, we can convert luminosity to density and analyze the probability that the authors would have observed an impact with a shell of a given ρ_{CSM} that occurred during their observations, illustrated in Figure 9. The same shell considered for CSM12 but at $R = 10^{16}$ cm, to account for the later observation time, would again escape detection at $\rho_{\text{CSM}} \approx 10^{-22} \text{ g cm}^{-3}$.

As we have shown here, by using the parameterized light curves and fiducial model relations one can easily quantify the probability of detecting shells spanning a range of f_R and ρ_{CSM} for a given set of observations. Alternatively, one could constrain for instance the ejecta velocity and f_R , and use Equation 16 to analyze the likelihood of detecting shells of varying radii and densities.

6. MULTIPLE SHELL COLLISIONS

We have demonstrated that the light curves of ejecta impacting a single shell form a family of solutions that can be straightforwardly applied to the interpretation of radio observations. In these simulations, we assume that there is negligible CSM interaction prior to the interaction being considered - i.e. the space between the supernova progenitor and the CSM shell is empty. However, it is natural to wonder how it would look if one shell collision was followed by another: could we simply add the light curves, preserving their convenient properties? In this section we perform this experiment and show that the light curves from multiple shell collisions differ dramatically from a simple addition of two single-shell light curves.

Imagine a system with two thin ($f_R = 0.1$) CSM shells: Shell 1 at 9.2×10^{14} cm with $\rho_{\text{CSM}} = 8.8 \times 10^{-15} \text{ g cm}^{-3}$ and Shell 2 at 7.7×10^{15} cm with $\rho_{\text{CSM}} = 4.7 \times 10^{-18} \text{ g cm}^{-3}$. The ejecta impacts Shell 1 at 5 days in a self-similar model, and if Shell 1 were not present the ejecta would impact Shell 2 at 50 days; therefore, models of the *single-shell* impact with these shells are called “1sh5” (Shell 1) and “1sh50” (Shell 2). The double-shell model (“2sh27”) is the same as 1sh5 until Shell 1 impacts Shell 2 on day 27. Note that the earlier impact time (27 days versus 50 days) is due to the fact that this second interaction starts not when the *ejecta* impacts Shell 2 but rather when *Shell 1* does, which happens earlier since Shell 1 is exterior to the ejecta. The initial condition of 2sh27 is the day-27 state of 1sh5 for $r < R_{1-2}$ plus the initial state of 1sh50 for $r > R_{1-2}$, where R_{1-2} is the contact discontinuity radius between the shells. The number of zones in the 1sh50 CSM was adjusted to match the mass resolution of 1sh5.

Figure 10 shows that the 2sh27 light curve is dramatically different than those of 1sh5 and 1sh50. First, the 2sh27 light curve is strikingly flat and broad, maintaining a luminosity similar to the peak luminosity of 1sh50 for nearly twenty days. Second, the light curve has an elbow at $t_{\text{exp}} = 41$ days (time C; corresponding to panel C of Figure 11). Note that in this figure, the 1sh5 light curve would in fact be subject to synchrotron self-absorption, an effect that we neglect here because it is not the interesting part of the evolution.

Since our 1-D simulations do not have mixing, we can calculate the luminosity contribution from the Shell 1 and Shell 2 zones separately (which zones belong to each

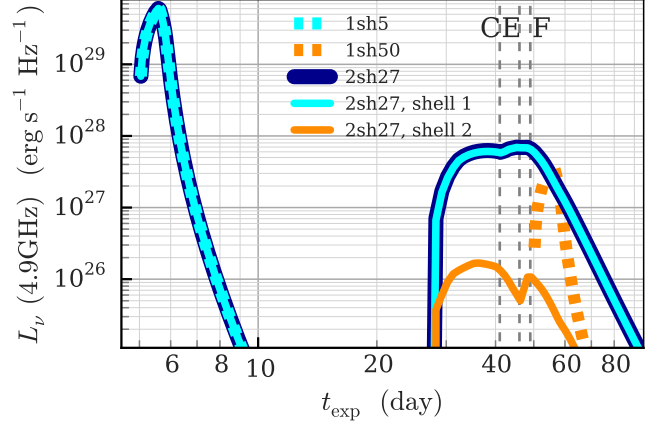


FIG. 10.— 4.9 GHz light curve of the two-shell model 2sh27 (navy). It can be broken down into the radiation from Shell 1 (cyan thin) and Shell 2 (orange thin); after impact with Shell 2, the signal from Shell 1 dominates in this band because the Shell 2 synchrotron spectrum peaks at a much lower frequency than Shell 1. Thick dashed lines show single-shell models: the light curves that would result from assuming that Shell 1 (1sh5; cyan; assuming optically thin to SSA) or Shell 2 (1sh50; orange) was the only shell in the system; simply summing these light curves is not at all a good approximation to the behavior of the two-shell system after impact with Shell 2. Compared to 1sh50, 2sh27 has a longer-lived and brighter light curve, with a plateau that lasts a couple of weeks and a more gradual decline. Dashed vertical lines indicate important features in the light curve: the elbow in Shell 1 (C), elbow in Shell 2 (E), and time of final descent (F), with letters corresponding to panels in Figure 11.

shell is known by construction, as illustrated in Figure 11). When separated into the contribution from each shell, we see that the light curve is dominated by the signal from Shell 1. This is simply because of the chosen frequency of $\nu_{\text{obs}} = 4.9$ GHz; in our model the ratio of cyclotron frequency in Shell 2 to Shell 1 is $\nu_{c,\text{sh2}}/\nu_{c,\text{sh1}} \sim 2\%$, thus $L_{\nu,\text{sh2}}/L_{\nu,\text{sh1}} \sim 2\%$. The Shell 2 light curve also has an elbow (time E; $t_{\text{exp}} = 44$ days) that occurs later than the Shell 1 elbow. Finally, both the Shell 1 and Shell 2 light curves start their final decline at $t_{\text{exp}} = 49$ days (time F).

This complicated light curve is caused by “sloshing” of shocks in Shell 1 which re-energize the gas for ~ 27 days, the dynamical time (Appendix A.1) This “sloshing” can be seen in snapshots of the simulation at critical times (Figure 11). Remember that Shell 1 dominates the signal in the following narrative of the interaction: (A) *Impact*. Shell 1 is much less dense than either the ejecta or Shell 2, and it is approaching Shell 2 at high speeds. (B-C) *Shock moves leftward through Shell 1*. When Shell 1 hits the “wall” of Shell 2, a shock forms. It energizes Shell 2 in a way reminiscent of single-shell evolution, breaking out quickly. (D) *Shock forms at ejecta-Shell 1 boundary and re-energizes Shell 1*. Because of the new shock, u_{gas} increases and the light curve has another small rise. (E) *Shock forms at the Shell 1-Shell 2 boundary, re-energizing both shells*. We see that when the shock moving through Shell 1 (seen in panel D) hits Shell 2, a new shock forms. The Shell 2 light curve begins a dramatic second rise and Shell 1 is able to maintain its luminosity. (F) *After a dynamical time the system has had time to adjust and the light curve begins to decline*. This panel shows a snapshot just before the decline of both light curves. Minor shocks continue to slosh inside shell 1 between the

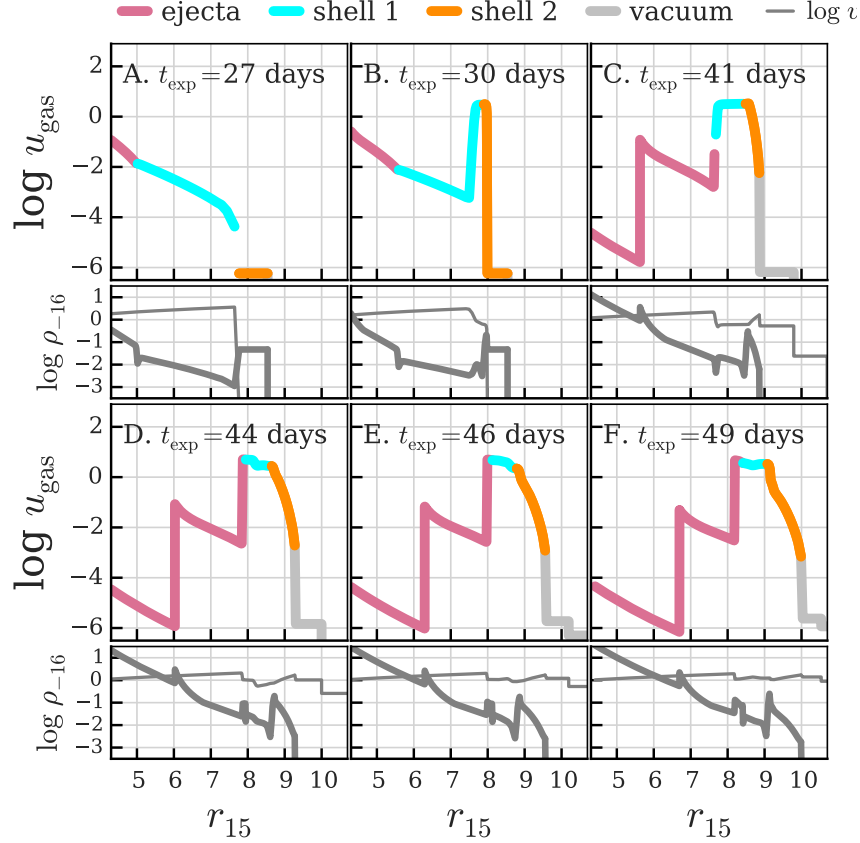


FIG. 11.— Like Figure 2. Snapshots of 2sh27 (double shell model) at important times in its evolution, showing u_{gas} in the ejecta (pink), Shell 1 (cyan), Shell 2 (orange), and the vacuum (light grey). The energy density in Shell 1 stays high because of “shock sloshing”: the recurring formation of shocks in Shell 1 caused by a shock front reaching either the ejecta on the left or Shell 2 on the right and forming a new shock front in Shell 1 that travels the opposite direction.

ejecta and shell 2, causing the more gradual light curve fall compared to single-shell models.

This is just one possible configuration of a double-shell system and its evolution probably does not generalize to the whole class of such collisions; however, it illustrates that the evolution of these systems is distinct from single-shell model evolution and so produces a radically different light curve. Note that higher-dimensional simulations may be required for investigating this class further because the significance of the “shock slosh” could be diminished by turbulence.

7. CONCLUSIONS

In order to quantitatively interpret the radio light curves and spectra of iSNe, one needs to understand the evolution of the shocked gas. One popular model for shock evolution is the Chevalier (1982, “C82”) one-dimensional self-similar interaction model, which assumes a continuous CSM. Here we explored moving beyond these models to the case of CSM shells (e.g. due to novae) in the low-density case where the shocked CSM does not cool and is optically thin. This removes the self-similar model assumption that the interaction has had time to reach self-similarity (i.e. that the CSM is close to the progenitor star or is very extended).

We created a suite of models to explore the parameter space of shell properties, focusing on shell density, thickness, and time of impact. In our “fiducial” mod-

els, we enforce an initial CSM-to-ejecta density ratio of $A_R = 0.33$ at the contact discontinuity (motivated by C82; Equation 5). If the shell were infinite, these models would evolve to the C82 self-similar solution (§ 2); however, because of the finite extent of the shells, self-similarity is never reached in our models.

We calculated synchrotron radio light curves for these models, since this emission traces the evolution of the shocked region only. We found a similar behavior among the radio light curves of fiducial models – they peak at a predictable time (Equation 8), have the same shape (Equation 11), and peak at a luminosity that can be calculated from shell characteristics (Equation 12). Therefore these light curves can be parameterized in a way that allows CSM properties to be inferred readily from an observed light curve (§ 3). In fact we find that shell properties can be approximated even if there is a higher initial density ratio (i.e. faster, lower density ejecta colliding with the shell) than is assumed in the fiducial set (§ 4).

We then showed how one can use the fiducial models to better interpret radio non-detections of SNe Ia by applying our work to the radio observations of SN 2011fe and SN 2014J (§ 5).

We presented a two-shell model to illustrate that our single shell light curves do not apply in that case, as a double shell light curve is much longer lived because of an effect that we call “shock sloshing” that occurs in

the first shell (§ 6). Shock sloshing produces elbows in the light curve that may be an observable signature of this behavior; exploring the diversity in multiple shell collisions is an enticing direction for future work.

Our fiducial model set is a new tool for studying the interaction of SNe Ia with a CSM, with the goal of constraining the supernova progenitor system. With the fiducial set, one can easily make observational predictions and analyze radio observations. Future work will focus on calculations of the radiation transport in the op-

tical and x-ray, to show how data at those wavelengths can reinforce radio constraints on supernovae interaction.

ACKNOWLEDGMENTS

The authors thank the anonymous referee for improving the clarity of this manuscript. C.E.H. is supported by the Department of Energy Computational Science Graduate Fellowship.

APPENDIX

APPENDIX

Diffusion and Cooling Timescale Estimates

We simulate the interaction between ejecta and CSM under the assumptions that (1) the gas is optically thin to electron scattering, so photons can free-stream through it and (2) the gas does not radiatively cool. To investigate the legitimacy of these assumptions, we can compare the timescale for dynamical changes (t_{dyn}) to the diffusion time (t_{diff}) and the cooling time (t_{cool}) in the forward shock region.

The dynamical time is

$$t_{\text{dyn}} = R/v \approx R_{c,0}/v_{\text{ej}} \approx t_{\text{imp}} \quad (\text{A1})$$

since the shocked gas is quickly accelerated to nearly the ejecta velocity and the ejecta is freely expanding.

The assumption that photons can free-stream requires that the diffusion time be much less than the dynamical time. The diffusion time for electron scattering through a shocked region of width ΔR_s and optical depth τ is

$$t_{\text{diff}} = \frac{\Delta R_s}{c} \min(\tau, 1) \quad (\text{A2})$$

Assuming that all species are fully ionized within the shocked region, the electron number density (n_e) and ion number density (n_I) are related to the mass density (ρ), atomic number (Z), atomic mass (A), and proton mass (m_p) through $n_e = Zn_I$ and $n_I = \rho/(Am_p)$, so the optical depth to electron scattering is

$$\tau = \sigma_T n_e \Delta R \approx (4 \times 10^{-3}) \left(\frac{Z}{A} \right) \rho_{s,-18} \Delta R_{s,16} \quad (\text{A3})$$

with $\rho_{s,-18}$ the density of the gas in the shocked region per $10^{-18} \text{ g cm}^{-3}$ and $\Delta R_{s,16}$ the width of the shocked region per 10^{16} cm . For the estimates here, we assume the gas is hydrogen dominated so $Z \approx A \approx 1$. Assuming a typical value for the shock width $\Delta R_s \approx 0.1 R_c$ and that the postshock density is related to the initial CSM density as $\rho_s \approx 4\rho_{\text{CSM}}$,

$$t_{\text{diff}} \approx (1 \text{ min}) R_{c,16}^2 \rho_{\text{CSM},-18} \quad (\text{A4})$$

The assumption that the shocked gas does not cool requires that the cooling time be much longer than the dynamical time. The cooling time for any radiative process is given by

$$t_{\text{cool}} = u_{\text{gas}}/(4\pi j) = 1.5 n k_B T/(4\pi j) \quad (\text{A5})$$

where u_{gas} is the gas internal energy density (which we have assumed is that of a monatomic ideal gas) and j is the angle-averaged, frequency-integrated emissivity of a radiative process. For free-free emission of thermal electrons, the angle-integrated emissivity (corresponding to $4\pi j$ in the above equation) is

$$j_{\text{ff}} = 1.43 \times 10^{-27} Z^2 n_I n_e T^{1/2} \bar{g}_B \quad (\text{A6})$$

in cgs units (Rybicki & Lightman 1979). Choosing a value of 1.2 for the gaunt factor \bar{g}_B gives an accuracy of about 20%. Using n_e, n_I as above and again assuming the shocked material has a density $\rho \approx 4\rho_{\text{CSM}}$ and $A = Z = 1$,

$$t_{\text{cool,ff}} \approx (1600 \text{ yr}) \rho_{\text{CSM},-18}^{-1} T_9^{1/2} \quad (\text{A7})$$

where $T_9 = T/(10^9 \text{ K})$. The strong shock jump conditions for an ideal gas link the temperature and shock velocity as

$$\frac{3}{2} \frac{\rho_{\text{CSM}}}{\mu m_p} k T_s = u_{\text{gas}} = \frac{P}{\gamma_{\text{ad}} - 1} = \frac{3}{2} \left(\frac{2}{\gamma_{\text{ad}} + 1} \rho_{\text{CSM}} v_s^2 \right) = 1.125 \rho_{\text{CSM}} v_s^2 \quad (\text{A8})$$

$$\Rightarrow T_9 \approx 9 \mu v_{s,9}^2 \quad (\text{A9})$$

where here $\gamma_{\text{ad}}=5/3$ is the adiabatic index and $v_{s,9} = v_s/(10^9 \text{ cm s}^{-1})$ is the shock velocity per 10,000 km s $^{-1}$. For our models we expect that v_s is similar to the ejecta velocity so $T_9 \sim 1 - 10$ and thus the cooling timescale is much longer than the dynamical timescale.

For the fiducial model set, we can use Equations 5 and A9 to recast the diffusion and cooling timescales in terms of physical parameters. Figure 1 illustrates these constraints and shows that our models obey them.

Luminosity Calculations

Synchrotron Emissivity

To calculate radio synchrotron light curves, we assume a fraction f_{NT} of electrons are accelerated into a non-thermal power law distribution $dn_e = C\gamma^{-p}d\gamma$ (with γ the electron Lorentz factor) with a total number density $n_{e,\text{NT}} = f_{\text{NT}}n_e$. Data for stripped-envelope core-collapse supernovae favors $p \approx 3$ (Chevalier & Fransson 2006). The normalization C is given by

$$n_{e,\text{NT}} = \int_{\gamma_{\min}}^{\infty} C\gamma^{-p}d\gamma \quad (\text{A10})$$

$$\Rightarrow C = n_{e,\text{NT}}(p-1)\gamma_{\min}^{p-1} \quad (\text{A11})$$

If a fraction ϵ_e of the shock energy went into accelerating the electrons (energy density u_e), then

$$u_e \equiv \epsilon_e u_{\text{gas}} = \int_{\gamma_{\min}}^{\infty} (\gamma m_e c^2) C\gamma^{-p}d\gamma \quad (\text{A12})$$

which we can combine with Equation A11 to show that

$$\gamma_{\min} = \frac{u_e}{n_{e,\text{NT}} m_e c^2} \left(\frac{p-2}{p-1} \right) \quad (\text{A13})$$

For the special case $p = 3$ which we assume in this work,

$$\gamma_{\min} = \frac{1}{2} \frac{u_e}{n_{e,\text{NT}} m_e c^2}, \quad (\text{A14})$$

$$C = \frac{1}{2} n_{e,\text{NT}} \left(\frac{u_e}{n_{e,\text{NT}} m_e c^2} \right)^2 \quad (\text{A15})$$

Assuming isotropic radiation, we can derive the synchrotron emissivity of these electrons as the power density per frequency per steradian

$$j_\nu(\nu > \nu_c) = \frac{1}{4\pi} \frac{1}{d\nu} n_e(\gamma) P_e(\gamma) = \frac{1}{4\pi} \frac{1}{d\nu} (C\gamma^{-p}d\gamma) P_{\text{syn}} \quad (\text{A16})$$

where P_{syn} is an electron's power output in synchrotron radiation

$$P_{\text{syn}}(\gamma) = \frac{4}{3} \sigma_T c u_B \gamma^2 \beta^2 \quad (\text{A17})$$

with u_B the magnetic field energy density ($u_B = B^2/8\pi$) and $\beta = v/c$. We parameterize the magnetic field energy density as $u_B = \epsilon_B u_{\text{gas}}$, as is common practice. The frequency of synchrotron radiation is related to the cyclotron frequency $\nu_c = eB/(2\pi m_e c)$ as

$$\nu = \gamma^2 \nu_c \quad (\text{A18})$$

thus

$$\frac{d\gamma}{d\nu} = (2\gamma\nu_c)^{-1} \quad (\text{A19})$$

Using Equations A17–A19 in Equation A16,

$$j_\nu(\nu > \nu_c) = \frac{\sigma_T c}{6\pi} C u_B \nu_c^{-1} \left(\frac{\nu}{\nu_c} \right)^{(1-p)/2} \quad (\text{A20})$$

where here we have assumed that $v \sim c$, with c the speed of light; to relax this assumption one would multiply the above by $(1 - \gamma^{-2})$. This is a slightly simpler version of the anisotropic equation given in Rybicki & Lightman (1979), and the two are equal to within a factor of order unity if one takes the pitch angle terms in the latter equation to be their angle-averaged value $\langle \sin \theta \rangle_\theta = 2/\pi$. For $p = 3$, we can use Equation A15 and our parameterizations $u_B = \epsilon_B u_{\text{gas}}$, $u_e = \epsilon_e u_{\text{gas}}$ to write this as

$$j_\nu(\nu > \nu_c \mid p = 3) = \frac{\sigma_T}{12\pi m_e^2 c^3} \epsilon_e^2 \epsilon_B n_e^{-1} u_{\text{gas}}^3 \nu^{-1}. \quad (\text{A21})$$

Assuming fully ionized hydrogen ($n_e = (Z/A)\rho/m_p$ with $Z/A = 1$ as described for Equation A3), this gives

$$j_\nu(\nu > \nu_c \mid p = 3) = (1.3 \times 10^{-15} \text{ erg s}^{-1} \text{ cm}^{-3} \text{ Hz}^{-1} \text{ sr}^{-1}) \left(\frac{\epsilon_e}{0.1}\right)^2 \left(\frac{\epsilon_B}{0.1}\right) \\ \times \left(\frac{\rho}{10^{-18} \text{ g cm}^{-3}}\right)^{-1} \left(\frac{u_{\text{gas}}}{10^2 \text{ erg cm}^{-3}}\right)^3 \left(\frac{\nu}{\text{GHz}}\right)^{-1} \quad (\text{A22})$$

For our simulations, we assume the CSM is solar composition and that only regions with $T > 10^4$ K radiate (and that these regions are fully ionized; recall that for times of interest the radiating regions have $T \sim 10^9$ K). The radiating region extends from the ejecta-CSM contact radius to the forward shock radius, which is identified by an algorithm that finds the sharp break in the u_{gas} profile (see, e.g. Figure 2). We calculate the luminosity by calculating the emissivity in each radiating zone (zone defined in § 2) scaled by its peak value (at ν_c), then multiplying by the volume of the zone and 4π steradians, as is appropriate in the optically thin limit. For a quantitative discussion of our optically thin assumption as it applies to synchrotron self-absorption, see § A.2.4.

As discussed in the main text, for a few models we consider the emission from the reverse shock region. This is calculated in the same manner except that the composition is assumed to be dominated by species heavier than hydrogen, in which case $A/Z = 2$.

Self-Similar Evolution Light Curve

Next we use the synchrotron emissivity to calculate the luminosity predicted from the C82 self-similar evolution. In the case of constant-density CSM, we can use our model parameters (see § 2, particularly Equation 1) in Equation 3 of C82 to derive that a self-similar shock has speed

$$R_1 = 1.131 R_c \quad (\text{A23})$$

$$\Rightarrow v_s = dR_1/dt = 0.792 R_c t^{-1} = 0.502 (M_{\text{ej}} v_t^7)^{1/7} R_c^{-3/7} \rho_{\text{CSM}}^{-1/7} \quad (\text{A24})$$

where R_1 is the radius of the forward shock front, v_s is the shock velocity, and as usual ρ_{CSM} is the preshock CSM density and R_c is the radius of the contact discontinuity. Substituting this into Equation A9,

$$u_{\text{gas}} = 1.125 \rho_{\text{CSM}} v_s^2 = 0.284 (M_{\text{ej}} v_t^7)^{2/7} R_c^{-6/7} \rho_{\text{CSM}}^{5/7}. \quad (\text{A25})$$

Thus the emissivity (Equation A21, with $\rho = 4\rho_{\text{CSM}}$), assuming fully ionized hydrogen gas, evolves like

$$j_\nu = 0.092 \frac{\sigma_T m_p}{12\pi m_e^2 c^3} (M_{\text{ej}} v_t^7)^{6/7} \epsilon_e^2 \epsilon_B \nu^{-1} R_c^{-18/7} \rho_{\text{CSM}}^{8/7} \quad (\text{A26})$$

and the emitting volume increases like

$$V = \frac{4\pi}{3} (R_1^3 - R_c^3) = 1.871 R_c^3 \quad (\text{A27})$$

which together produce

$$\mathcal{L}_{\nu, \text{ss}} \sim j_\nu V \sim 0.17 \frac{\sigma_T m_p}{12\pi m_e^2 c^3} (M_{\text{ej}} v_t^7)^{6/7} \epsilon_e^2 \epsilon_B \nu^{-1} R_c^{3/7} \rho_{\text{CSM}}^{8/7}. \quad (\text{A28})$$

For our model parameters of $M_{\text{ej}} = 1.38 M_\odot$, $v_t = 1.022 \times 10^9 \text{ cm s}^{-1}$, $\epsilon_e = \epsilon_B = 0.1$,

$$\mathcal{L}_{\nu, \text{ss}} \sim (2.3 \times 10^{29} \text{ erg s}^{-1} \text{ Hz}^{-1}) \left(\frac{\nu}{\text{GHz}}\right)^{-1} R_{c,16}^{3/7} \rho_{\text{CSM},-18}^{8/7} \quad (\text{A29})$$

where $R_{c,16} = R_c/(10^{16} \text{ cm})$ is the current contact discontinuity radius and $\rho_{\text{CSM},-18} = \rho_{\text{CSM}}/(10^{-18} \text{ g cm}^{-3})$. From Equation 5, we see that $R_c^{3/7} \propto t^{3/10}$ so the scaling of luminosity with time is

$$\mathcal{L}_{\nu, \text{ss}} \propto t^{0.3} \quad (\text{A30})$$

Adiabatic Losses Light Curve

After several dynamical times (Equation A1) have passed since shock breakout, the system should have relaxed into a state of free expansion, with $R \propto t$. In this state, we expect adiabatic evolution of the gas,

$$V \propto R^3 \propto t^3 \quad (\text{A31})$$

$$p \propto V^{-5/3} \Rightarrow u_{\text{gas}} \propto V^{-5/3} \propto t^{-5}. \quad (\text{A32})$$

This produces a decline in the emissivity

$$j_\nu \propto \rho^{-1} u_{\text{gas}}^3 \propto t^{-12} \quad (\text{A33})$$

so in this state of free expansion we have

$$L_\nu \propto j_\nu V \propto t^{-9}. \quad (\text{A34})$$

This explains why the decline in the radio light curves is so steep after shock breakout.

Synchrotron Self-Absorption

The relativistic electrons that create synchrotron emission can also absorb synchrotron radiation in a process known as synchrotron self-absorption (SSA). From Rybicki & Lightman (1979), the extinction coefficient for SSA is

$$\alpha_{\text{SSA}} = \frac{\sqrt{3}q^3}{8\pi m_e} \left(\frac{3q}{2\pi m^3 c^5} \right)^{p/2} C_E (B \sin \theta)^{(p+2)/2} \Gamma \left(\frac{3p+2}{12} \right) \Gamma \left(\frac{3p+22}{12} \right) \nu^{-(p+4)/2} \quad (\text{A35})$$

where Γ is the gamma function and C_E is from $n(E) = C_E E^{-p} dE$ and is thus related to the C of Equation A11 by $C_E = (mc^2)^{p-1} C$. We have used $p = 3$ in the second expression. As previously mentioned, the $\sin \theta$ term is a pitch angle term that is attached to the magnetic field amplitude B and thus carried through the derivation. In our situation, we expect both the magnetic fields and the electron velocities to be randomly oriented and therefore when using synchrotron equations from Rybicki & Lightman (1979), we adopt the angle-averaged value $B \sin \theta = B \langle \sin \theta \rangle_\theta = (2/\pi)B$. Thus with some substitution we can write this as

$$\alpha_{\text{SSA}} = \frac{1}{64} \left(\frac{6}{\pi} \right)^{(p+3)/2} \Gamma \left(\frac{3p+2}{12} \right) \Gamma \left(\frac{3p+22}{12} \right) \frac{\sigma_{TC}}{m_e} u_B C \nu_B^{(p-2)/2} \nu^{-(p+4)/2} \quad (\text{A36})$$

$$= (4.74 \times 10^{-7} \text{ cm}^{-1}) \left(\frac{\epsilon_e}{0.1} \right)^2 \left(\frac{\epsilon_B}{0.1} \right)^{5/4} \times \left(\frac{\rho}{10^{-18} \text{ g cm}^{-3}} \right)^{-1} \left(\frac{u_{\text{gas}}}{10^2 \text{ erg cm}^{-3}} \right)^{13/4} \left(\frac{\nu}{\text{GHz}} \right)^{-7/2} \quad (\text{A37})$$

where ρ is the mass density of the shocked gas and u_{gas} its internal energy density.

We can estimate the optical depth of a model by assuming α_{SSA} is uniform in the shocked gas. With $\mu \approx 1$ and $\rho = 4\rho_{\text{CSM}}$ the energy density is

$$u_{\text{gas}} \approx \frac{6\rho_{\text{CSM}}}{m_p} k_B T \approx 0.5 \rho_{\text{CSM},-18} T_9 \quad (\text{A38})$$

so

$$\alpha_{\text{SSA}} \approx (1.6 \times 10^{-14} \text{ cm}^{-1}) \rho_{\text{CSM},-18}^{2.25} T_9^{3.25} \nu_9^{-3.5} \quad (\text{A39})$$

where $\nu_9 = \nu/\text{GHz}$. Assuming the shocked region has a width $\Delta R_s \sim 0.1 R_c$ then

$$\tau_{\text{SSA}} \sim 0.1 \alpha_{\text{SSA}} R_c \quad (\text{A40})$$

$$\sim 16 R_{c,16} \rho_{\text{CSM},-18}^{2.25} T_9^{3.25} \nu_9^{-3.5}. \quad (\text{A41})$$

The optical depth of a model varies with time because of these dependencies on temperature and radius, but we show the line of $\tau = 1$ in Figure 1 assuming $T_9 = 20$ and $\nu_9 = 4.9$ for reference.

When fiducial models are optically thin such that the synchrotron luminosity is set by the emissivity, their light curves obey scaling relations that reflect the similar hydrodynamic evolution of the models as described in § 3. As the models become more optically thick, the light curve is set by the source function $S_{\nu,\text{SSA}}$, which from Equations A22 and A37 we calculate to be

$$S_{\nu,\text{SSA}} = \frac{j_\nu}{\alpha_{\text{SSA}}} = (2.8 \times 10^{-9} \text{ erg s}^{-1} \text{ cm}^{-2} \text{ Hz}^{-1} \text{ sr}^{-1}) \times \left(\frac{u_B}{10 \text{ erg cm}^{-3}} \right)^{-1/4} \left(\frac{\nu}{\text{GHz}} \right)^{-5/2}. \quad (\text{A42})$$

For arbitrary optical depth, the luminosity of a one-dimensional numerical model can be found via the formal solution of the radiative transfer equation using this source function.

REFERENCES

- Bloom, J. S., Kasen, D., Shen, K. J., Nugent, P. E., Butler, N. R., Graham, M. L., Howell, D. A., Kolb, U., Holmes, S., Haswell, C. A., Burwitz, V., Rodriguez, J., & Sullivan, M. 2012, *ApJ*, 744, L17
- Cao, Y., Kulkarni, S. R., Howell, D. A., Gal-Yam, A., Kasliwal, M. M., Valenti, S., Johansson, J., Amanullah, R., Goobar, A., Sollerman, J., Taddia, F., Horesh, A., Sagiv, I., Cenko, S. B., Nugent, P. E., Arcavi, I., Surace, J., Woźniak, P. R., Moody, D. I., Rebbapragada, U. D., Bue, B. D., & Gehrels, N. 2015, *Nature*, 521, 328
- Castor, J. I. 2007, *Radiation Hydrodynamics*
- Chevalier, R. A. 1982, *ApJ*, 258, 790
- Chevalier, R. A. 1996, in *Astronomical Society of the Pacific Conference Series*, Vol. 93, *Radio Emission from the Stars and the Sun*, ed. A. R. Taylor & J. M. Paredes, 125
- Chevalier, R. A. & Fransson, C. 1994, *ApJ*, 420, 268
- . 2006, *ApJ*, 651, 381
- Chomiuk, L., Soderberg, A. M., Moe, M., Chevalier, R. A., Rupen, M. P., Badenes, C., Margutti, R., Fransson, C., Fong, W.-f., & Dittmann, J. A. 2012, *ApJ*, 750, 164

- Dilday, B., Howell, D. A., Cenko, S. B., Silverman, J. M., Nugent, P. E., Sullivan, M., Ben-Ami, S., Bildsten, L., Bolte, M., Endl, M., Filippenko, A. V., Gnat, O., Horesh, A., Hsiao, E., Kasliwal, M. M., Kirkman, D., Maguire, K., Marcy, G. W., Moore, K., Pan, Y., Parrent, J. T., Podsiadlowski, P., Quimby, R. M., Sternberg, A., Suzuki, N., Tytler, D. R., Xu, D., Bloom, J. S., Gal-Yam, A., Hook, I. M., Kulkarni, S. R., Law, N. M., Ofek, E. O., Polishook, D., & Poznanski, D. 2012, *Science*, 337, 942
- Gerardy, C. L., Höflich, P., Fesen, R. A., Marion, G. H., Nomoto, K., Quimby, R., Schaefer, B. E., Wang, L., & Wheeler, J. C. 2004, *ApJ*, 607, 391
- Kasen, D. 2010, *ApJ*, 708, 1025
- Marcaide, J. M., Alberdi, A., Ros, E., Diamond, P., Shapiro, I. I., Guirado, J. C., Jones, D. L., Mantovani, F., Pérez-Torres, M. A., Preston, R. A., Schilizzi, R. T., Sramek, R. A., Trigilio, C., Van Dyk, S. D., Weiler, K. W., & Whitney, A. R. 1997, *ApJ*, 486, L31
- Margutti, R., Soderberg, A. M., Chomiuk, L., Chevalier, R., Hurley, K., Milisavljevic, D., Foley, R. J., Hughes, J. P., Slane, P., Fransson, C., Moe, M., Barthelmy, S., Boynton, W., Briggs, M., Connaughton, V., Costa, E., Cummings, J., Del Monte, E., Enos, H., Fellows, C., Feroci, M., Fukazawa, Y., Gehrels, N., Goldsten, J., Golovin, D., Hanabata, Y., Harshman, K., Krimm, H., Litvak, M. L., Makishima, K., Marisaldi, M., Mitrofanov, I. G., Murakami, T., Ohno, M., Palmer, D. M., Sanin, A. B., Starr, R., Svinkin, D., Takahashi, T., Tashiro, M., Terada, Y., & Yamaoka, K. 2012, *ApJ*, 751, 134
- Moore, K. & Bildsten, L. 2012, *ApJ*, 761, 182
- Nugent, P. E., Sullivan, M., Cenko, S. B., Thomas, R. C., Kasen, D., Howell, D. A., Bersier, D., Bloom, J. S., Kulkarni, S. R., Kandrashoff, M. T., Filippenko, A. V., Silverman, J. M., Marcy, G. W., Howard, A. W., Isaacson, H. T., Maguire, K., Suzuki, N., Tarlton, J. E., Pan, Y.-C., Bildsten, L., Fulton, B. J., Parrent, J. T., Sand, D., Podsiadlowski, P., Bianco, F. B., Dilday, B., Graham, M. L., Lyman, J., James, P., Kasliwal, M. M., Law, N. M., Quimby, R. M., Hook, I. M., Walker, E. S., Mazzali, P., Pian, E., Ofek, E. O., Gal-Yam, A., & Poznanski, D. 2011, *Nature*, 480, 344
- Panagia, N., Van Dyk, S. D., Weiler, K. W., Sramek, R. A., Stockdale, C. J., & Murata, K. P. 2006, *ApJ*, 646, 369
- Parrent, J. T., Howell, D. A., Friesen, B., Thomas, R. C., Fesen, R. A., Milisavljevic, D., Bianco, F. B., Dilday, B., Nugent, P., Baron, E., Arcavi, I., Ben-Ami, S., Bersier, D., Bildsten, L., Bloom, J., Cao, Y., Cenko, S. B., Filippenko, A. V., Gal-Yam, A., Kasliwal, M. M., Konidaris, N., Kulkarni, S. R., Law, N. M., Levitan, D., Maguire, K., Mazzali, P. A., Ofek, E. O., Pan, Y., Polishook, D., Poznanski, D., Quimby, R. M., Silverman, J. M., Sternberg, A., Sullivan, M., Walker, E. S., Xu, D., Buton, C., & Pereira, R. 2012, *ApJ*, 752, L26
- Patat, F., Chugai, N. N., Podsiadlowski, P., Mason, E., Melo, C., & Pasquini, L. 2011, *A&A*, 530, A63
- Pérez-Torres, M. A., Lundqvist, P., Beswick, R. J., Björnsson, C. I., Muxlow, T. W. B., Paragi, Z., Ryder, S., Alberdi, A., Fransson, C., Marcaide, J. M., Martí-Vidal, I., Ros, E., Argo, M. K., & Guirado, J. C. 2014, *ApJ*, 792, 38
- Roth, N. & Kasen, D. 2015, *ApJS*, 217, 9
- Rybicki, G. B. & Lightman, A. P. 1979, *Radiative processes in astrophysics*
- Silverman, J. M., Nugent, P. E., Gal-Yam, A., Sullivan, M., Howell, D. A., Filippenko, A. V., Arcavi, I., Ben-Ami, S., Bloom, J. S., Cenko, S. B., Cao, Y., Chornock, R., Clubb, K. I., Coil, A. L., Foley, R. J., Graham, M. L., Griffith, C. V., Horesh, A., Kasliwal, M. M., Kulkarni, S. R., Leonard, D. C., Li, W., Matheson, T., Miller, A. A., Modjaz, M., Ofek, E. O., Pan, Y.-C., Perley, D. A., Poznanski, D., Quimby, R. M., Steele, T. N., Sternberg, A., Xu, D., & Yaron, O. 2013, *ApJS*, 207, 3
- Silverman, J. M., Vinkó, J., Marion, G. H., Wheeler, J. C., Barna, B., Szalai, T., Mulligan, B. W., & Filippenko, A. V. 2015a, *MNRAS*, 451, 1973
- . 2015b, *MNRAS*, 451, 1973
- Soderberg, A. M., Berger, E., Page, K. L., Schady, P., Parrent, J., Pooley, D., Wang, X.-Y., Ofek, E. O., Cucchiara, A., Rau, A., Waxman, E., Simon, J. D., Bock, D. C.-J., Milne, P. A., Page, M. J., Barentine, J. C., Barthelmy, S. D., Beardmore, A. P., Bietenholz, M. F., Brown, P., Burrows, A., Burrows, D. N., Byrnes, G., Cenko, S. B., Chandra, P., Cummings, J. R., Fox, D. B., Gal-Yam, A., Gehrels, N., Immler, S., Kasliwal, M., Kong, A. K. H., Krimm, H. A., Kulkarni, S. R., Maccarone, T. J., Mészáros, P., Nakar, E., O’Brien, P. T., Overzier, R. A., de Pasquale, M., Racusin, J., Rea, N., & York, D. G. 2008, *Nature*, 453, 469
- Warren, J. S., Hughes, J. P., Badenes, C., Ghavamian, P., McKee, C. F., Moffett, D., Plucinsky, P. P., Rakowski, C., Reynoso, E., & Slane, P. 2005, *ApJ*, 634, 376
- Wood-Vasey, W. M. & Sokoloski, J. L. 2006, *ApJ*, 645, L53